




ORIGINAL RESEARCH ARTICLE

Aluminum Substitution in Ni-Co Based Spinel Ferrite Nanoparticles by Sol–Gel Auto-Combustion Method

MUNIBA,¹ MUHAMMAD KHALID,^{2,7} ALI DAD CHANDIO,⁵
MUHAMMAD SAEED AKHTAR ^{4,8} JUNAID KAREEM KHAN,¹
GHULAM MUSTAFA,¹ NAIMAT ULLAH CHANNA,⁶
ZAHEER ABBAS GILANI,³ and HM NOOR UL HUDA KHAN ASGHAR³

1.—Department of Physics, NED University of Engineering and Technology, Karachi 75270, Pakistan. 2.—Department of Physics, University of Karachi, Karachi 75270, Pakistan. 3.—Department of Physics, Balochistan University of Information Technology, Engineering and Management Sciences, Quetta 87300, Pakistan. 4.—Department of Physics, University of Education, Lahore, Pakistan. 5.—Department of Metallurgical Engineering, NED University of Engineering and Technology, Karachi 75270, Pakistan. 6.—Department of Physics, Shah Abdul Latif University, Khairpur 66111, Pakistan. 7.—e-mail: khalid.mesp@gmail.com. 8.—e-mail: saeed.akhtar@ue.edu.pk

In this research work, aluminum substituted Ni-Co ferrite nanoparticles have been produced by a simple and cost-effective method, i.e., sol–gel auto-combustion. Synthesized nanoparticles were annealed in a muffle furnace at 600°C for 3 h before characterization. The x-ray diffraction patterns revealed that the ferrite nanoparticles grew preferentially along the (311) plane and exhibit face centered cubic structure. The crystallite size of nanoparticles (14 to 17 nm) was estimated by Scherrer's relation. The effect of aluminum substitution on structural parameters of ferrite nanoparticles, such as lattice constant and stacking faults, have been studied. Structural analysis revealed that the lattice constant of the nanoparticles decreases as a function of aluminum content. The Fourier transform infrared spectroscopy confirmed the spinel ferrite crystal structure of synthesized aluminum substituted Ni-Co ferrite nanoparticles. The surface morphology observed through scanning electron microscopy depicts the growth and distribution of nanograins with uniform size with in the samples. Dielectric properties investigated through impedance analyzer spectroscopy revealed that aluminum substituted Ni-Co ferrite nanoparticles demonstrated the high conductivity along with potential dielectric properties. These aluminum substituted Ni-Co ferrite nanoparticles would have possible applications in high storage memory and microwave devices.

Key words: Sol–gel, spinel ferrites, crystal structure, surface morphology, dielectric properties

INTRODUCTION

Metal oxide nanoparticles have an important role in numerous fields of nanoscience and technology.¹ Metal oxides are the most abundant minerals found in earth's crust. Spinel ferrite is a large group of

materials with many applications such as storage devices, sensors, magnetic drug delivery, electronics and microwaves.^{2–5} A spinel structure is a unit cell with 56 ions, 32 are of oxygen and 24 are metal. Spinel ferrite is an important structural class of oxides with interesting properties and a wide range of applications. The general formula of spinel type oxides is AB_2O_4 with face centered cubic structure, where A and B represent the di- and trivalent ions or quadrivalent cations including aluminum,

(Received October 9, 2020; accepted February 12, 2021; published online March 16, 2021)

manganese, zinc, magnesium, titanium, chromium etc. If the spinel structure consists of iron as one of the major components, the oxides are termed ferrites. The magnetic spinel ferrite nanoparticles can be used as drug carriers inside the body and are capable of addressing the limitations of conventional drug delivery systems in medical science⁶.

The cation distribution in spinel ferrites would result to promising electrical and magnetic properties. The overall Fe^{+3} and divalent metal ion distribution at sites (tetrahedral-octahedral) govern the properties of spinel ferrites, e.g., sensing the species of a gas mixture. There are several other parameters that can significantly influence the spinel ferrite's properties such as size of crystallites, stoichiometry and morphology. These factors are observed to be sensitive to the synthesis procedure.⁷ Several chemical and physical methods have been employed to synthesize ferrite nanoparticles, especially mechanical milling,⁸ plastic deformation consolidation,⁹ inert gas condensation,¹⁰ coprecipitation,¹¹ sol-gel,¹²⁻¹⁷ mechano-chemical, microwave assisted,^{18,19} solid state reaction,²⁰ reverse micelle, solvothermal, hydrothermal and micro-emulsion²¹⁻²⁵ methods.

In the present study, aluminum doped nickel cobalt (Ni-Co) spinel ferrite nanoparticles were synthesized using a simple and cost-effective sol-gel auto-combustion technique. The aluminum substituted Ni-Co spinel ferrite nanoparticles were analyzed using XRD, FTIR, SEM and LCR meter to investigate the structural, morphological and electrical properties for their possible applications in sensing and microwave applications.

EXPERIMENTAL METHODOLOGY

Chemical Synthesis

The nickel cobalt ferrite powders, $\text{NiCoFe}_{2-x}\text{Al}_x\text{O}_4$, with x varying from 0 to 0.4, were synthesized by sol-gel auto-combustion. Analytical grade cobalt (II) nitrate ($\text{Co}(\text{NO}_3)_2$), nickel (II) nitrate ($\text{Ni}(\text{NO}_3)_2$), iron (III) nitrate hexahydrate ($\text{Fe}(\text{NO}_3)_3 \cdot 9\text{H}_2\text{O}$), and aluminum (V) nitrate $\text{Al}(\text{NO}_3)_3 \cdot 9\text{H}_2\text{O}$ were used as starting materials. The initial solutions were prepared by dissolving nitrates of metal and citric acid in de-ionized water with molar ratio of 1:2. Vigorous stirring of metal nitrate mixture in a thermostatic water bath at 80°C resulted in formation of dry gel followed by continuous addition of citric acid. The prepared gel was then dried for 2 h in an oven at 120°C . The powder obtained was then burnt and ground followed by sintering at specific temperatures. The structural, microstructural, and dielectric characterization of spinel ferrite nanoparticles were carried out through x-ray diffraction (XRD), FTIR, SEM and impedance analyzer have been carried out. Structural properties of prepared nanoparticles were investigated using a PANalytical x-ray diffractometer with $\text{Cu-K}\alpha$ ($\lambda = 1.5406 \text{ \AA}$) radiation and

equipped with X'Pert Pro software. FEI NOVA 450 NanoSEM was employed to investigate the microstructure of the prepared nanoparticles. A NicoletTM iS50 spectrometer was used to collect FTIR spectra for a range of frequency (400 to 1000 cm^{-1}). Electrical characteristics were examined with the help of 6520P Wayne Kerr LCR meter for frequency ranging from 1 Hz to 20 MHz . For electrical measurements, the powder samples were pressed hydraulically under a force of 5 t for 2 min to prepare pallets with thickness and diameter as ~ 2.5 and $\sim 7.5 \text{ mm}$, respectively. Front and back silver contacts of 200 nm thickness were deposited before electrical characterization. The influence of humidity was minimized by drying the nanoparticles at 100°C in vacuum.

RESULTS AND DISCUSSIONS

Structural Investigations

X-ray Diffraction

The x-ray diffraction (XRD) patterns of aluminum substituted Ni-Co spinel ferrites are shown in Fig. 1. All the observed diffraction peaks are well matched with standard JCPDS card # 01-077-0426. The substantial change in the crystallite size of aluminum substituted ferrite nanoparticles was observed. The crystallite size for powder samples was estimated using diffraction peak arises from the (311) plane. It has been observed that up to 20 % substitution of aluminum in the lattice of Ni-Co lattice, the structural parameters would not alter significantly. The following structural parameters have been calculated from XRD results and are listed in Table I.

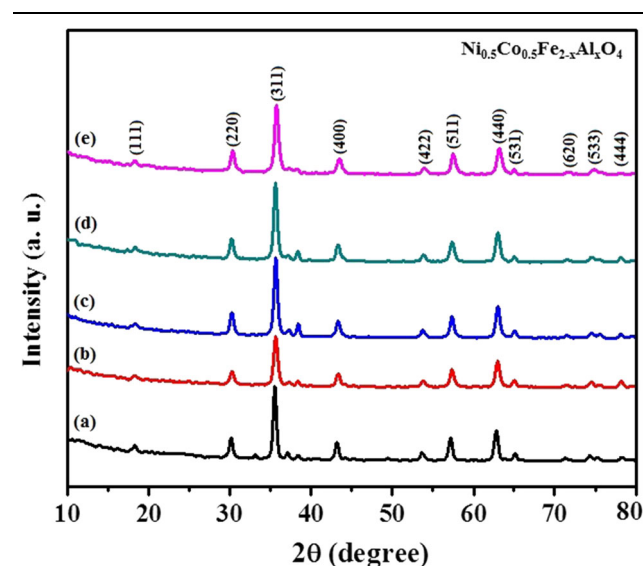


Fig 1. XRD patterns of Al substituted Ni-Co based spinel ferrite with aluminum content as $x = 0.0$ (b) $x = 0.1$ (c) $x = 0.2$ (d) $x = 0.3$ and (e) $x = 0.4$.

Crystallite Size

Crystallite size (D) was calculated by Debye–Scherrer’s equation

$$D = \frac{0.95\lambda}{\beta \cos \theta}, \quad (1)$$

where Θ is the angle of diffraction, β is full width at half maximum and λ is the wavelength of incident x-rays.

Lattice Spacing

Lattice spacing was calculated by Bragg’s Law

$$d = \frac{n\lambda}{2 \sin \theta}, \quad (2)$$

where d is the distance between atomic planes and n is the order of diffraction taken as 1.

Dislocation Density

$$\delta = \frac{1}{D^2}, \quad (3)$$

where D is the crystallite size.

Dislocation density is the overall dislocation length per unit volume of crystal structure. Annealing of samples reduces the dislocation density and strength; however, improving the grain size. Using annealing, the strength and ductility of crystal arrangement can be controlled. The dislocations can be parallel lines or simply the random lines appearing in the crystal. There is an inverse relation between dislocation density and particle size. The type of defects present in the synthesized samples are probably the linear defects.

Lattice Constants

For the calculation of lattice constant, the values of Miller indices, i.e. h (3), k (1), and l (1) were used. By substituting the value of Miller indices and inter-planer spacing d, the lattice constant can be calculated as ²⁶;

$$a = d\sqrt{h^2 + k^2 + l^2} \quad (4)$$

Lattice Strain

When pressure is applied, the unit length of an object deforms, expressing the strain in the samples. The atoms possess slight variation in the normal lattice positions due to creation of defects in crystal structure and imperfections in crystal structure²⁷. These imperfections in the structure include interstitial and/or impurity atoms resulting in lattice strain.

$$\varepsilon = \frac{\beta}{4 \tan \theta}, \quad (5)$$

where β is the full width at half maximum of diffraction peak (in radians).

Micro-Strain

Deformation that is caused in one part per million (10^{-6}) of the material is usually caused by dislocations, plastic deformation, point defects that occur in the crystal structure and the defects in domain boundaries.²⁸ One essential aspect of micro-strain is that it provides peak broadening which is shown by the following equation:

$$\varepsilon = \frac{\beta \cos \theta}{4}, \quad (6)$$

where Θ is the angle of diffraction and β is the full width at half maximum

Stacking Faults

Stacking faults are the disturbances in normal lattice structure that arises in layered arrangement or fault that is occurred in the atomic planes of the crystal.²⁹

$$\text{Stacking fault} = \frac{2\pi^2}{45\sqrt{3} \tan \theta} \quad (7)$$

The variation in various structural parameters as a function of aluminum substitution is given in Figs. 2 and 3.

Figure 2 shows the aluminum concentration dependent crystallite size and lattice constant. It is clear from the figure that both the crystallite size and lattice constant decrease with increasing aluminum

Table I. Structural parameters of Ni-Co based spinel ferrite nanoparticles

Parameters	x = 0.0	x = 0.1	x = 0.2	x = 0.3	x = 0.4
d-spacing (Å)	2.524	2.516	2.517	2.518	2.509
Lattice constant (Å)	8.373	8.347	8.348	8.354	8.323
Crystallite size (nm)	17	14	15	15	14
Cell Volume (Å ³)	587.14	581.64	581.827	583.034	576.720
Lattice strain (x 10 ⁻³)	6.784	8.21	7.43	7.353	8.267
Dislocation density (x 10 ¹⁵) (lines/m ²)	3.565	5.254	4.303	4.208	5.359
Stacking Fault	0.44	0.44	0.44	0.44	0.44
Micro-strain x 10 ⁻³ (lines ⁻² /m ⁻⁴)	2.069	2.512	2.273	2.248	2.536
X-ray density (g cm ⁻³)	5.304	5.289	5.221	5.145	5.135
Bulk density (g cm ⁻³)	2.995	2.989	2.987	2.972	2.965

concentration. The values of crystallite were found in the range from 17 to 14 nm while the lattice constant was found to decrease from 8.373 to 8.323 Å with increasing Al doping³⁰. The obtained results are in good agreement with published data for cubic spinel ferrites nanoparticles. The decrease in both crystallite size and lattice constant with increasing in aluminum concentration can be explained on the basis of difference in their ionic radius of Fe (0.67 Å) and Al (0.57 Å) ions. The decrease in the lattice constant is due to the replacement of large Fe³⁺ ions with smaller Al³⁺ ions³¹.

The x-ray density of prepared nanoparticles³² was calculated from the relation as given below ,

$$\rho_x = \frac{8M}{N_A a^3}, \tag{8}$$

where, ρ_x represents the x-ray density to be calculated, M represents the molecular mass of the sample, N_A is Avogadro's number (6.023×10^{23}) and a is obviously the lattice constant. The bulk density for the ferrite nanoparticles has been calculated from the given relation³³.

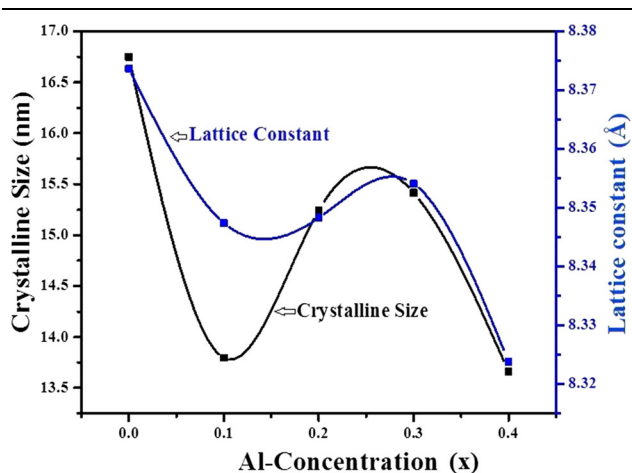


Fig 2. Variation in lattice constant and crystalline size of Ni_{0.5}Co_{0.5}Al_xFe_{2-x}O₄ (x = 0.0, 0.1, 0.2, 0.3, 0.4) nanoparticles.

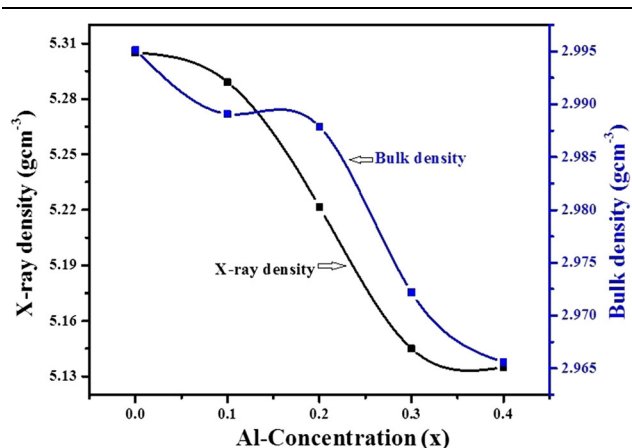


Fig 3. Variation in x-ray and bulk density of Ni_{0.5}Co_{0.5}Al_xFe_{2-x}O₄ (x = 0.0, 0.1, 0.2, 0.3, 0.4) nanoparticles.

$$\rho_m = \frac{m}{\pi r^2 t} \tag{9}$$

The x-ray and bulk density as function Al³⁺ content in Ni_{0.5}Co_{0.5}Al_xFe_{2-x}O₄ spinel ferrite is shown in Fig. 3. It is clear that both bulk and x-ray density decreases with an increase in Al³⁺ concentrations. The reason for decreasing the both type densities is that the atomic weight of Al³⁺ is smaller than that of Fe³⁺. In Eq. 8, the decrease in molecular mass causes the decrease in x-ray density because there is a significant impact of molecular mass rather than the negligible decrease of the lattice constant. Furthermore, the decrease in bulk density is contributing to the mass of pallets, as is clear from Eq. 9. As the aluminum concentration increases, the mass of the pallets decrease which ultimately reduces the bulk density. By enhancing the dopant's (Al³⁺) concentration, a decrease in the bulk and x-ray density was observed from 2.995 to 2.965 g/cm³ and from 5.304 to 5.134 g/cm³, respectively.

FTIR Study

Fourier transform infrared (FTIR) spectroscopy was performed to verify the structure of spinel phase in all the prepared samples. From FTIR analysis, information about cation distribution in all sites (tetrahedral and octahedral) in a crystal and chemical changes that occurred in the composition has been gathered. Figure 4 depicts the FTIR spectra taken in the frequency range from 400 to 1000 cm⁻¹ for Ni-Co based spinel ferrites. Two frequency bands have been recorded, one at 500 cm⁻¹ which is a high-frequency band (ν_1) and the other at 400 cm⁻¹ which is low energy band (ν_2). The ν_1 band observed to increase from 521 to 539 cm⁻¹ and ν_2 band observed to decrease from 429 to 411 cm⁻¹. The absorption peaks are due to tetrahedral site of intrinsic stretching vibration of metal. Low-

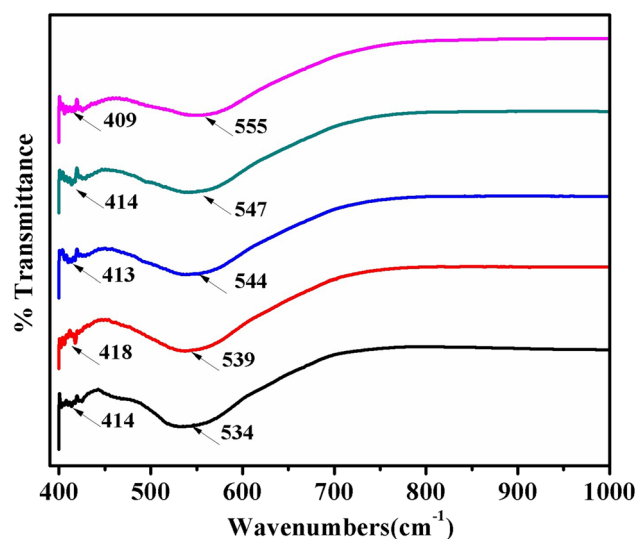


Fig 4. FTIR spectra of Al doped Ni-Co spinel ferrite nanoparticle.

frequency bands ν_2 belong to octahedral metal stretching bands. The stretching vibration of $\text{Fe}^{3+}-\text{O}^{2-}$ on tetrahedral and octahedral sites is due to change in lattice parameter. The shift of band ν_2 toward lower frequency is due to the increasing aluminum concentration. The lattice constant firstly increased followed by a slight decrease in the present work owing to the stretching vibration of $\text{Fe}^{3+}-\text{O}^{2-}$. This plays a vital role in deviating the position of bonds. The above given figure shows the two frequency bands and provides the evidence of successful doping of aluminum in nickel ferrites. Table II illustrates the high-frequency band ν_1 and low-frequency band ν_2 . As the values of ν_1 absorbed peaks are shifting toward higher values, the low-frequency bands are shifting toward lower frequency bands. From the figure, it is clear that band shifting observed with the changing concentration of aluminum might be due to cations on tetrahedral and octahedral positions.

The K_o and K_t , force constants were calculated for tetrahedral and octahedral positions by using following relations.

$$K_o = 0.942128M(V_2)^2/M + 32 \quad (10)$$

$$K_t = 2^{1/2}k_o\nu_1/\nu_2, \quad (11)$$

where M represents the molecular weight. The tetrahedral and octahedral radii were also obtained from the given formula³⁴;

$$R_{\text{tetra}} = a(3)^{1/2}(u - 0.25) \quad (12)$$

$$R_{\text{octa}} = a(5/8 - u) - R_o, \quad (13)$$

where u represents the oxygen position parameter, R_{tetra} and R_{octa} are tetra- and octahedral radii, respectively, and a is a lattice constant. The value of the oxygen position parameter is 0.375.

Microstructural Analysis

Scanning electron microscopy (SEM) of aluminum doped Ni-Co based spinel ferrite nanoparticles revealed the surface morphology, grain size, and their distribution. Well-crystallized grains of $\text{Ni-CoAl}_x\text{Fe}_{2-x}\text{O}_4$ with uniform size have been grown. The average grain size of $\text{Ni-CoFe}_2\text{O}_4$ and Ni-

$\text{CoAl}_{0.1}\text{Fe}_{0.9}\text{O}_4$ was measured using ImagJ software and found to be 137.5 and 130.5 nm, respectively. The microstructural analysis is in strong agreement with the XRD data. Agglomeration of the grain can also be seen at some surface areas of the samples. The existence of smaller grains is evidence for the large surface-to-volume ratio of the prepared samples. It has also been observed that the morphology of synthesized nanoparticles depends on the aluminum content in the samples. The substitution of aluminum resulted in agglomeration of smaller grains due to the magnetic interactions between the neighboring particles. This deterioration to some extent in morphology of the grown material does not mean the degradation of the prepared ferrite sample. This might be due to liberation gases on aluminum inclusion during the crystallization. This accumulation or aggregation of nanoparticles is depicted in Fig. 5. Stoichiometrically increase of x values causes to decrease in the stoichiometric rate of Fe atoms in the molecular structure of the ferrite. It was observed from the SEM assessment that the aggregation of the nanoparticles varies depending on the stoichiometric rate of Fe atoms. Some planar or spinal shapes seen on SEM micrographs, especially when x value is 0.2. In the other micrograph, the aggregations among ferrite nanoparticles are random, although their visible shape is powdery. This formation attributed to the mass balance between aluminum and Fe atoms. Lower or higher stoichiometric rate of aluminum on Fe resulted in smaller nanoparticle formation in addition to the limited growth caused by the difference in ionic radii and internal stress.

Dielectric Properties

Information of any material about the conduction mechanisms, dielectric relaxation and polarization behavior can be extracted from its dielectric characteristics. The permeability and permittivity may alter with frequency, orientation of crystallites, temperature, composition, molecular structure and pressure.³⁵

Dielectric Constant

The measurement of dielectric constant (frequency dependent) was carried out in the frequency

Table II. Parameters extracted from the FTIR spectra of Al doped Ni-Co based spinel ferrite nanoparticle

Parameters	$x = 0.0$	$x = 0.1$	$x = 0.2$	$x = 0.3$	$x = 0.4$
Molecular weight (g/mol)	2354.503	231.616	228.730	225.844	222.957
ν_1 (cm^{-1})	534	539	544	547	555
ν_2 (cm^{-1})	414	418	413	414	409
K_o (dyne/cm^2) $\times 10^5$	1.420	1.446	1.409	1.414	1.378
K_t (dyne/cm^2) $\times 10^5$	2.591	2.631	2.626	2.642	2.644
R_o	0.773	0.766	0.767	0.768	0.760
R_t	1.812	1.807	1.807	1.808	1.802

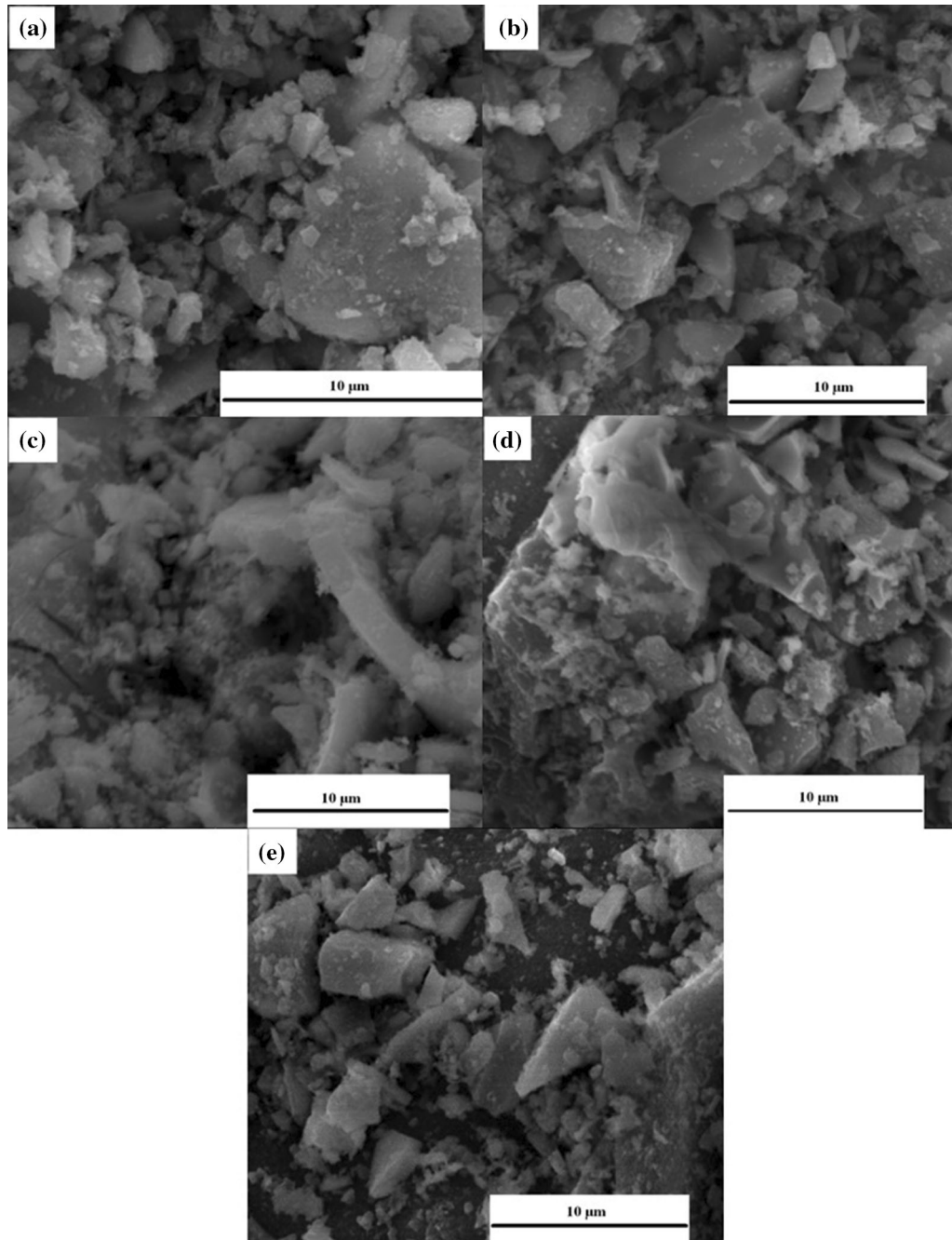


Fig 5. SEM micrographs of Al doped Ni-Co based spinel ferrite nanoparticle: (a) $x = 0.0$, (b) $x = 0.1$, (c) $x = 0.2$, (d) $x = 0.3$ and (e) $x = 0.4$.

range from 20 Hz to 20 MHz. The prepared samples were placed between two electrodes attached to a measuring setup at room temperature with an applied current of 5 mA. The equivalent parallel resistance (R_p) and parallel capacitance (C_p) were calculated for all samples by using the following relation;³⁶

$$\varepsilon' = \frac{C \times d}{A \times \varepsilon_0}, \quad (14)$$

where ε' represents the dielectric constant, C represents the capacitance, d represents the pallet's

thickness, ε_0 represents the permittivity of the free space and A represents the area of prepared pallets. The real and imaginary dielectric constants are shown in Figs. 6 and 7, respectively, for spinel ferrite nanoparticles, and all the dielectric parameters are listed in Table III.

These dielectric measurements can be deduced through the impact of grain boundaries and electrical properties of the samples. However, the characteristic peaks that correspond to the aluminum content in to Ni-Co samples revealed that dielectric constants are strongly dependent on the factors

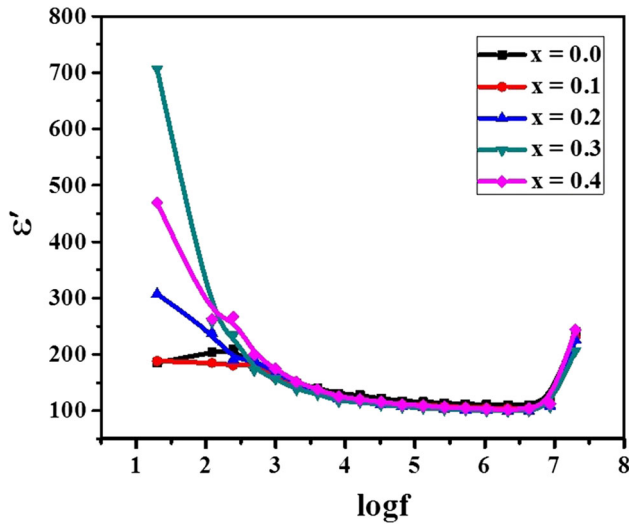


Fig 6. Real dielectric constant of Al doped Ni-Co based spinel ferrite nanoparticles.

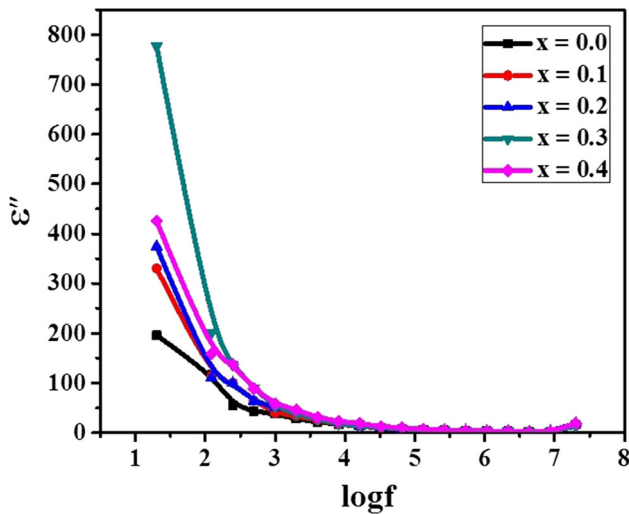


Fig 7. Imaginary dielectric constant of Al doped Ni-Co based spinel ferrite nanoparticles.

such as electronic dipolar, ionic and space charge contributions. The analysis of dielectric constant revealed that its values are dominant over low frequencies and the reason could be distinct types of polarization (dipolar or space charge) caused by permanent dielectric moments of the molecules.³⁷ Moreover, the dielectric constant observed to decrease at higher frequency range. The reason for this reduction could be the decrement in the significant contribution from the space charge and ionic polarization.³⁴

Tangent Loss Study

Figure 8 shows the variation of frequency and tangent loss at different concentrations of aluminum in the ferrite samples. The tangent loss

was observed to decrease as a function of increasing frequency. This observation indicated the behavior of ferrites. At a certain frequency, the jumping charge carriers cannot follow the alternation of AC field. At higher doping level, the dielectric loss decreases. At high frequency the AC conductivity of the material also increases with increasing energy of electrons³⁸.

Impedance Spectroscopy

The impedance analysis is necessary to understand the role of grain boundaries and electrode potential. The impedance analysis actually relates the electrical process that takes place with the samples as reported earlier.^{39,40}

The complex impedance was measured as $Z^* = Z' - jZ''$ where Z' and Z'' are real and imaginary parts of impedance, respectively, which can be represented as.⁴¹

$$Z' = \frac{R_g}{1 + (\omega R_g C_g)^2} + \frac{R_{gb}}{1 + (\omega R_{gb} C_{gb})^2} \quad (15)$$

$$Z'' = \frac{R_g}{1 + (\omega R_g C_g)^2} + \frac{R_{gb}}{1 + (\omega R_{gb} C_{gb})^2}, \quad (16)$$

where ω represents the angular frequency, R_g represents the grain resistance, C_{gb} represents the grain boundary capacitance, C_g represents the grain capacitance and R_{gb} represents the grain boundary resistance.

Figures 9 and 10 represent the Nyquist plots of the aluminum substituted Ni-Co based nanoparticles. These plots consist of dispersion on the imaginary axis expressing a non-Debye type relaxation behavior. The Nyquist plots actually represent two different regions, one is the lower frequency grain boundary region and the other is higher frequency grain region.

Modulus Analysis

The electrical transport phenomenon depends significantly on the hopping rate of ions and conductivity relaxation time of considered samples⁴². The complex modulus of materials would help to understand the electrical transport phenomenon. The complex modulus formulation is bit advantageous over impedance spectroscopy as far as discrimination between grain boundary conduction and electrode polarization is concerned⁴³⁻⁴⁶.

Complex function of electric modulus can be written in terms of

$$M^* = M' + jM'' \quad (17)$$

The real and imaginary parts of the complex modulus can be expressed as

Table III. Dielectric parameters of Al doped Ni-Co based spinel ferrite nanoparticles

Parameters	Frequency	ϵ'	ϵ''	Tan (δ)	Z'	Z''	M'	M''
$X = 0.0$	10 kHz	161	38	0.234699	9.68×10^5	4.12×10^6	0.005879	0.00138
	50 kHz	120	8	0.071132	8.33×10^3	1.17×10^5	0.008312	0.000591
	20 MHz	240	16	0.067726	9.81	1.45×10^2	0.004148	0.000281
$X = 0.1$	10 kHz	158	40	0.252404	1.05×10^6	4.16×10^6	0.005935	0.001498
	50 kHz	113	8	0.072835	9.05×10^3	1.24×10^5	0.008814	0.000642
	20 MHz	231	16	0.068284	1.03×10^1	1.51×10^2	0.004315	0.000295
$X = 0.2$	10 kHz	168	50	0.301541	1.16×10^6	3.84×10^6	0.00547	0.00165
	50 kHz	110	10	0.090561	1.15×10^4	1.27×10^5	0.009041	0.000819
	20 MHz	226	19	0.083746	1.28×10^1	1.53×10^2	0.004388	0.000367
$X = 0.3$	10 kHz	157	52	0.330389	1.33×10^6	4.03×10^6	0.005749	0.001899
	50 kHz	108	8	0.076418	9.91×10^3	1.30×10^5	0.009199	0.000703
	20 MHz	207	13	0.062583	1.05×10^1	1.68×10^2	0.004812	0.000301
$X = 0.4$	10 kHz	175	58	0.332105	1.20×10^6	3.62×10^6	0.005156	0.001712
	50 kHz	113	10	0.090284	1.12×10^4	1.24×10^5	0.008781	0.000793
	20 MHz	244	18	0.074838	1.07×10^1	1.42×10^2	0.004078	0.000305

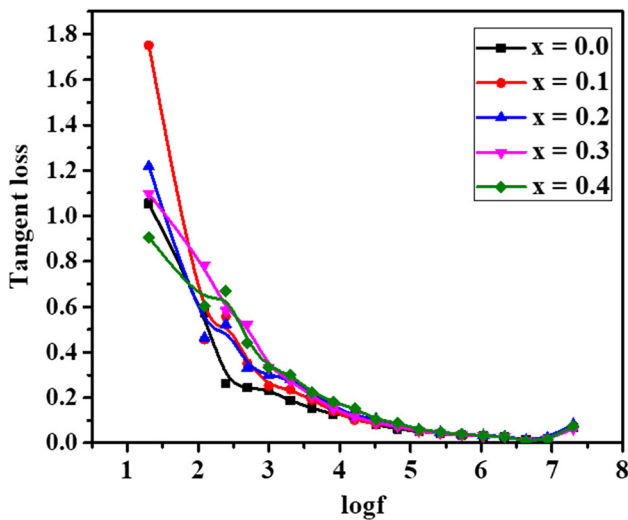


Fig 8. Frequency dependent tangent loss of Al doped Ni-Co based spinel ferrite nanoparticles.

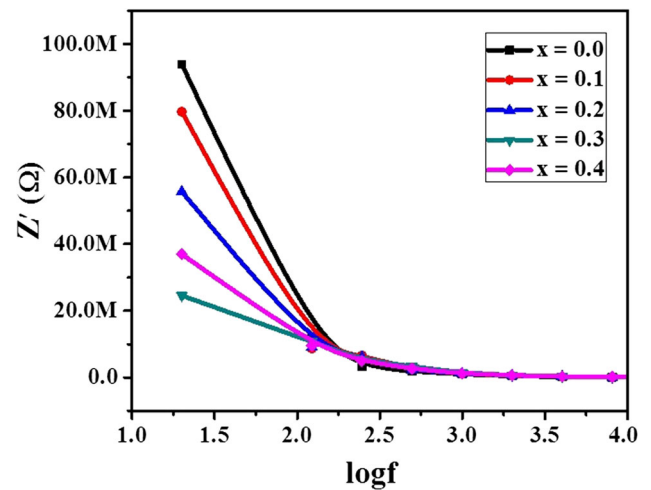


Fig 10. Real part of impedance versus log f (Hz) curves for Al doped Ni-Co based spinel ferrite nanoparticle.

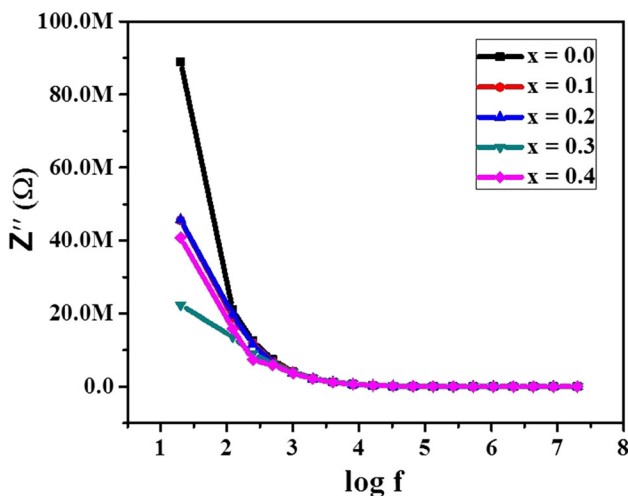


Fig 9. Imaginary part of impedance versus log f (Hz) curves for Al doped Ni-Co based spinel ferrite nanoparticle.

$$M' = \frac{\epsilon'}{\epsilon'^2 + \epsilon''^2} \tag{18}$$

$$M'' = \frac{\epsilon''}{\epsilon'^2 + \epsilon''^2}, \tag{19}$$

where ϵ' and ϵ'' are real and imaginary parts of the dielectric permittivity.

Figure 11 shows the variation of real part of modulus (M') with respect to frequency at different concentrations of aluminum in the ferrite samples. Figure 11 revealed that at lower frequencies, the M' is very low while at higher frequency, M' continuously increases until M^∞ .³⁷ At lower frequencies, charge carriers are mobile due to applied electric field and activation of electrode polarization. However, M' exhibits smaller values at various concentrations and its magnitude decreases as concentration increases due to weak restoring force

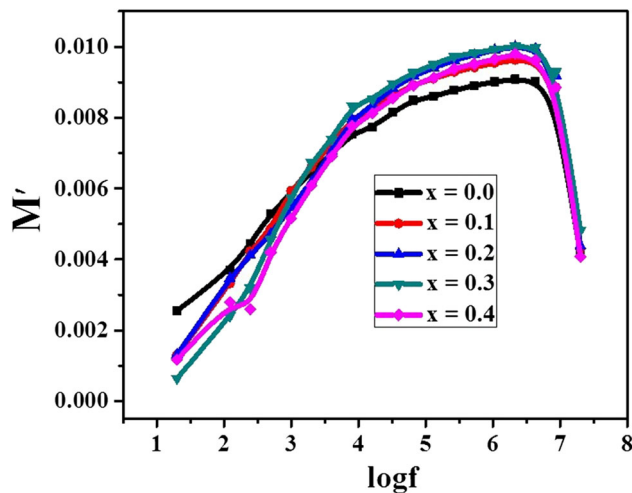


Fig 11. Real part of modulus for Al doped Ni-Co based spinel ferrite nanoparticles.

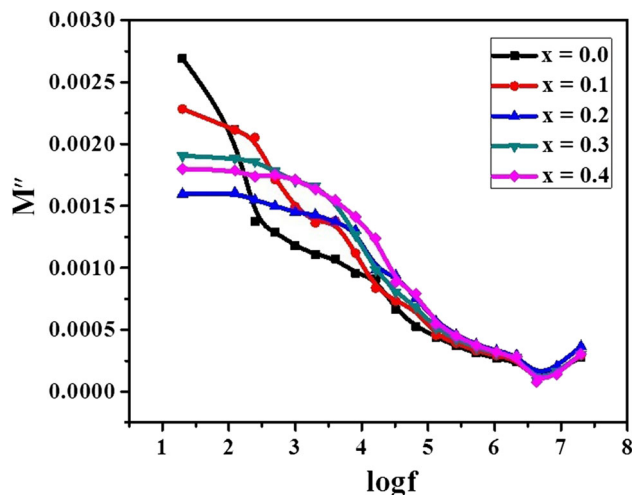


Fig 12. Imaginary part of modulus for Al doped Ni-Co based spinel ferrite nanoparticles.

at lower frequencies. Similar behavior for imaginary part of M has been observed as shown in Figure 12.

CONCLUSIONS

In summary, nickel-cobalt based aluminum substituted ferrite ($\text{NiCoFe}_{2-x}\text{Al}_x\text{O}_4$) nanoparticles have been synthesized successfully by a simple sol-gel auto-combustion method with five different concentrations of aluminum ($x = 0.0, 0.1, 0.2, 0.3$ and 0.4). The XRD patterns confirmed that prepared nanoparticles have been grown with preferred orientation along the (311) plane. The crystallite size was calculated by Scherrer's formula and lies in the range of 14 to 17 nm. The nanoparticles with observed range of crystallite size would have applications in cancer treatment, hyperthermia, drug delivery and magnetic storage devices. FTIR analysis revealed that the presence of functional groups

at octahedral and tetrahedral sites confirm the spinel nature of synthesized ferrite nanoparticles. Surface morphology revealed the growth of nanoparticles with uniform size and distribution. Dielectric properties confirm the frequency dependence of parameters like tangent loss, dielectric constant. The aluminum substituted Ni-Co based spinel ferrite nanoparticles with higher values of conductivity might have applications in many advanced electronic devices.

CONFLICT OF INTEREST

The authors declare that they have no conflict of interest.

REFERENCES

1. J.L.G. Fierro, *Metal oxides: chemistry and applications* (Boca Raton: CRC Press, 2005).
2. D. Chen, D. Chen, X. Jiao, Y. Zhao, and M. He, *Powder Technol.* 133, 247 (2003).
3. X. Shi, S.H. Wang, S.D. Swanson, S. Ge, Z. Cao, M.E. Van Antwerp, K.J. Landmark, and J.R. Baker Jr., *Adv. Mater.* 20, 1671 (2008).
4. J. Hong, D. Xu, J. Yu, P. Gong, H. Ma, and S. Yao, *Nanotechnology* 18, 135608 (2007).
5. J.H. Park, G. von Maltzahn, L. Zhang, M.P. Schwartz, E. Ruoslahti, S.N. Bhatia, and M.J. Sailor, *Adv. Mater.* 20, 1630 (2008).
6. K. Maaz, S. Karim, A. Mumtaz, S. Hasanain, J. Liu, and J. Duan, *J. Magn. Magn. Mater.* 321, 1838 (2009).
7. T.W. Mammo, C.V. Kumari, S.J. Margarete, A. Ramakrishna, R. Vemuri, Y.B. ShankarRao, K.L. Vijaya Prasad, Y. Ramakrishna, and N. Murali, *Phys. B* 581, 411769 (2020).
8. A. Ponce, E. Chagas, R. Prado, C. Fernandes, A. Terezo, and E. Baggio-Saitovitch, *J. Magn. Magn. Mater.* 344, 182 (2013).
9. R.Z. Valiev, R.K. Islamgaliev, and I.V. Alexandrov, *Prog. Mater. Sci.* 45, 103 (2000).
10. H.-E. Schaefer, H. Kisker, H. Kronmüller, and R. Würschum, *Nanostruct. Mater.* 1, 523 (1992).
11. P. Chand, S. Vaish, and P. Kumar, *Phys. B* 524, 53 (2017).
12. S.S. Ebrahimi, and J. Azadmanjiri, *J Non-Cryst Solids* 353, 802 (2007).
13. P. Sivakumar, R. Ramesh, A. Ramanand, S. Ponnusamy, and C. Muthamizhchelvan, *Mater. Res. Bull.* 46, 2204 (2011).
14. A. Ghasemi, X. Liu, and A. Morisako, *J. Magn. Magn. Mater.* 316, e105 (2007).
15. D.S. Mathew, and R.-S. Juang, *Chem. Eng. J.* 129, 51 (2007).
16. P. Priyadharsini, A. Pradeep, P.S. Rao, and G. Chandrasekaran, *Mater. Chem. Phys.* 116, 207 (2009).
17. M.N. Akhtar, A.A. Khan, M.N. Akhtar, M. Ahmad, and M.A. Khan, *Phys. B* 561, 121 (2019).
18. M. Sertkol, Y. Köseoğlu, A. Baykal, H. Kavas, and M.S. Toprak, *J. Magn. Magn. Mater.* 322, 866 (2010).
19. T.K. Bromho, K. Ibrahim, H. Kabir, M.M. Rahman, K. Hasan, T. Ferdous, H. Taha, M. Altarawneh, and Z.-T. Jiang, *Mater. Res. Bull.* 97, 444 (2018).
20. Z. Zhang, G. Yao, X. Zhang, J. Ma, and H. Lin, *Ceram. Int.* 41, 4523 (2015).
21. S. Deka, and P. Joy, *J. Am. Ceramic. Soc.* 90, 1494 (2007).
22. Z. Wang, Y. Xie, P. Wang, Y. Ma, S. Jin, and X. Liu, *J. Magn. Magn. Mater.* 323, 3121 (2011).
23. A. Ghasemi, and M. Mousavinia, *Ceram. Int.* 40, 2825 (2014).
24. E. Şentürk, Y. Köseoğlu, T. Şaşmaz, F. Alan, and M. Tan, *J. Alloy. Compd.* 578, 90 (2013).
25. M. Sertkol, Y. Köseoğlu, A. Baykal, H. Kavas, and A. Başaran, *J. Magn. Magn. Mater.* 321, 157 (2009).

26. P.-F. Yin, L.-L. Sun, Y.-L. Gao, and S.-Y. Wang, *B Mater Sci* 31, 593 (2008).
27. K. Krishnamoorthy, G.K. Veerasubramani, and S.J. Kim, *Mat. Sci. Semicon. Proc.* 40, 781 (2015).
28. L. Kumar, P. Kumar, A. Narayan, and M. Kar, *Int. Nano Lett.* 3, 8 (2013).
29. P. Solanki, S. Vasant, and M. Joshi, *Int. J. Appl. Ceram. Technol.* 11, 663 (2014).
30. K.V. Kumar, D. Paramesh, and P.V. Reddy, *World J. Nano Sci. Eng.* 5, 68 (2015).
31. Q. Lin, Y. He, J. Xu, J. Lin, Z. Guo, and F. Yang, *Nanomater. Basel* 8, 750 (2018).
32. Z. Wu, M. Okuya, and S. Kaneko, *Thin Solid Films* 385, 109 (2001).
33. A. Raut, R. Barkule, D. Shengule, and K. Jadhav, *J. Magn. Magn. Mater.* 358, 87 (2014).
34. R.S. Yadav, I. Kuřitka, J. Vilcakova, J. Havlica, J. Masilko, L. Kalina, J. Tkacz, J. Švec, V. Enev, and M. Hajdúchová, *Adv. Nat. Sci. Nanosci.* 8, 045002 (2017).
35. J. Joshi, D. Kanchan, M. Joshi, H. Jethva, and K. Parikh, *Mater. Res. Bull.* 93, 63 (2017).
36. D.C. Sinclair, *Bol. Soc. Esp. Ceram. V* 34, 55 (1995).
37. V. Tukaram, S.S. Shinde, R.B. Borade, and A.B. Kadam, *Phys. B* 577, 411783 (2020).
38. A.K. Jonscher, *Nature* 267, 673 (1977).
39. D.E. Gavrilă, *J Mater. Sci. Eng.* 4, 18 (2014).
40. R. Gimenes, M. Baldissera, M. Da Silva, C. Da Silveira, D. Soares, L.A. Perazolli, M. Da Silva, and M. Zaghete, *Ceram. Int.* 38, 741 (2012).
41. K. Hayat, M. Rafiq, S. Durrani, and M. Hasan, *Phys. B* 406, 309 (2011).
42. Y.B. Taher, A. Oueslati, N. Maaloul, K. Khirouni, and M. Gargouri, *Appl. Phys. A* 120, 1537 (2015).
43. K. Prasad, K. Kumari, K. Chandra, K. Yadav, and S. Sen, *Mater. Sci. Pol.* 27, 373 (2009).
44. T. Badapanda, V. Senthil, S. Rout, L. Cavalcante, A.Z. Simões, T. Sinha, S. Panigrahi, M. De Jesus, E. Longo, and J.A. Varela, *Curr. Appl. Phys.* 11, 1282 (2011).
45. K. Kumari, A. Prasad, and K. Prasad, *Am. J. Mater. Sci.* 6, 1 (2016).
46. M.M. Hossen, and M.B. Hossen, *Phys. B* 585, 412116 (2020).

Publisher's Note Springer Nature remains neutral with regard to jurisdictional claims in published maps and institutional affiliations.